

Available online at www.sciencedirect.com

ScienceDirect

journal homepage: www.elsevier.com/locate/he

Numerical simulation of the power-based efficiency in vanadium redox flow battery with different serpentine channel size

Jonghyeon Lee ^a, Jungmyung Kim ^a, Heesung Park ^{b,*}

^a Graduate School of Mechanical Engineering, Changwon National University, 51140, South Korea

^b Department of Mechanical Engineering, Changwon National University, 51140, South Korea

ARTICLE INFO

Article history:

Received 20 November 2018

Received in revised form

19 April 2019

Accepted 1 May 2019

Available online 30 May 2019

Keywords:

Numerical simulation

Vanadium redox flow battery

Serpentine channel

Power-based efficiency

ABSTRACT

We present numerical investigations on the power-based efficiency of vanadium redox flow battery (VRFB). A three-dimensional numerical model is developed to capture the complexities of electrochemical reactions and fluid dynamics when considering different serpentine channel sizes and electrolyte flow rates. It is shown that the reduced channel size and increased electrolyte flow rate improve the electrochemical performance of the VRFB due to the enhanced distribution of molar concentration at the electrodes. Nonetheless, the channel size reduction and increased electrolyte flow rate also increases pressure drop between inlet and outlet of the serpentine channels for negative and positive sides. In this, we calculate the power-based efficiency by considering the generated power of VRFB and power loss due to overpotentials, ohmic loss, and required pump power. The maximum power-based efficiency of 96.6% is calculated with the channel size of 1.9 mm at 60 mL min⁻¹, while it is 95.5% with 9.6 mm in channel size at 100 mL min⁻¹. The proposed numerical approach can be useful to determine the channel size with optimized electrolyte flow rate and maximum VRFB efficiency.

© 2019 Hydrogen Energy Publications LLC. Published by Elsevier Ltd. All rights reserved.

Introduction

Recently, the demand for environmental-friendly electrical power generation grows rapidly. Renewable energy resources of solar and wind have been developed to meet the increasing the demand [1–4]. Nonetheless, most of renewable energy can be intermittently supplied due to the change of the atmospheric conditions [5,6]. In this regard, redox flow batteries (RFBs) have attracted an increasing interest as an energy storage system which can be integrated with other renewable energy technologies [7–9]. The RFBs offer many advantages of long service life, high round-trip efficiency, and design

flexibility of energy and power ratings [8,10–14]. Although many different types of RFB exist, all-vanadium redox flow batteries (VRFBs) are most commonly developed due to the benefits of high capacity and reliability. For example, megawatt-scale VRFB systems have been demonstrated [15–19]. The oxidation/reduction reactions of the vanadium species occur at the positive and negative electrodes for the charging and discharging the VRFBs. This leads to excellent electrochemical reversibility [20–25]. Although the systematic efficiency and power density of the VRFBs are still critical issues for further commercialization, a large number of recent studies has been conducted to resolve the issues. Yang et al. [26] investigated the effect of operating parameters on the

* Corresponding author.

E-mail address: heesungpark@changwon.ac.kr (H. Park).

<https://doi.org/10.1016/j.ijhydene.2019.05.013>

0360-3199/© 2019 Hydrogen Energy Publications LLC. Published by Elsevier Ltd. All rights reserved.

performance of vanadium redox flow battery during discharging. They revealed that the discharging voltage was increased by increasing the initial vanadium concentration, initial acid concentration and electrolyte flow rate. Membrane characterization during cycle test was investigated by Zhang et al. [27]. They suggested that prevention of vanadium ions crossover significantly improved the energy efficiency of VRFB. Meanwhile, Dassisti et al. [28] presented thermal stability, cyclic voltammetry and electrochemical impedance measurements to assess the life cycles. The effect of sulfuric acid solution on vanadium electrolyte was investigated to obtain optimum electrochemical composition for VRFB [29]. In addition, optimum amount of additives was derived to reduce thermal precipitation of positive electrolyte of VRFB [30]. Tang et al. [31] developed the simulation model for stacked vanadium redox flow batteries. They optimized the electrolyte flow rate to achieve maximum systematic efficiency. The effect of electrolyte flow rate on vanadium redox flow battery performance was investigated by Khazaeli et al. [8]. They demonstrated that the increased electrolyte flow rate from 10 to 70 mL min⁻¹ improved 50 mV more cell voltage. Houser et al. [32] proposed that the serpentine flow field offered higher performance of VRFB than interdigitated flow fields. Their numerical model provided further design optimization by calculating the effect of convective mass transfer through the flow field. Xu et al. [33] also numerically simulated the performance of VRFBs with considering the flow fields. They found that the inclusion of flow fields in VRFBs improved 5% higher energy efficiency than without flow fields. Another study was also conducted to optimize the mass transfer with minimising the pressure drop in VRFB [34]. They concluded that the serpentine flow field was more suitable for VRFBs than parallel flow field in terms of power-based and round-trip efficiencies. Kim et al. reported numerical simulation of VRFB with considering the operating condition [35]. The design of electrolyte flow field in VRFB have been investigated by previous studies, however, the optimal and specific dimensions of the serpentine flow field has not been reported yet.

A three-dimensional numerical model based on computational fluid dynamics and electrochemical reactions is developed. In this work, we propose a method to find the optimal dimensions of the serpentine flow field by simulating the performance of VRFB. It is denoted that the improved electrical power by using serpentine flow field should be compromised with the consumed power to supply the electrolytes through the flow field. To do this, the electrolyte flow rate is varied from 40 to 100 mL min⁻¹, while the width of serpentine flow field is changed from 1.9 to 9.6 mm. As a result, the numerical simulations predict the maximum power-based efficiency when the VRFB operates under the flow rate of 60 mL min⁻¹ with serpentine flow field.

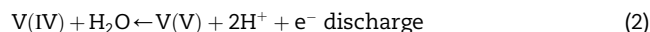
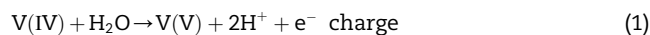
Numerical

Electrochemical reactions

Fig. 1 shows the schematic diagram of a single VRFB cell. A single cell (5 × 5 cm²) consisted of two electrodes separated by

the membrane, and two current collectors outside the electrodes. Electrolyte flow fields are designed at the current collectors to uniformly supply the electrolytes. The electrolytes consist of sulphuric acid solutions and vanadium ions. Positive and negative electrolytes are stored in the reservoirs and circulated by pumps. The electrochemical reactions occurred at the electrodes during charging/discharging of VRFB. The basic electrochemical reactions in VRFBs were expressed as follows:

At positive electrode:



At negative electrode:



It is denoted that V(II), V (III), V (IV), and V (V) are ionic species of V²⁺, V³⁺, VO²⁺, VO₂⁺.

As shown in Eqs. (1)–(4), the oxidation and reduction occurred at the positive and negative electrodes under the charge/discharge processes. Therefore, the total vanadium ions concentration remained constant during charging/discharging process. The state of charge (SOC) is defined by the concentrations of vanadium ions. In addition, the variation of SOC with time (t) is also calculated by using Eq. (5).

$$\text{SOC} = \frac{C_{\text{V(II)}}}{C_{\text{V(III)}} + C_{\text{V(II)}}} = \frac{C_{\text{V(V)}}}{C_{\text{V(IV)}} + C_{\text{V(V)}}} = s_0 + \frac{t}{t_0} (s_e - s_0) \quad (5)$$

where *c* and *t*₀ are molar concentration of each species and total charge/discharge time, while *s*₀ and *s*_e represent the SOC_s at the beginning and end of charge/discharge, respectively [36].

Governing equations

The governing equations are defined by using the equations of species, mass, momentum, and electrochemical reactions. The mass conservation equation of species in VRFB is expressed as:

$$\frac{\partial}{\partial t} (\epsilon C_i) + \nabla \cdot \vec{N}_i = -S_i \quad (6)$$

where ϵ and *c* represent the porosity of electrode and concentration, while \vec{N} and *S* are the molar flux and source term, respectively. The subscripts of *l* and *i* represent electrolyte and species, respectively. Source terms are given in Table 1 by Faraday constant (*F*) and current density (*j*) [11]. The concentration of SO₄²⁻ is calculated according to the electrical neutrality condition with valence (*z*) as expressed [37].

$$\sum_i z_i C_i = 0 \quad (7)$$

Diffused flow at the porous electrode is calculated by the Nernst-Planck equation.

$$\vec{N}_i = -D_{i,\text{eff}} \nabla C_i - z_i \kappa_i F C_i \nabla \phi_1 + \vec{u} C_i \quad (8)$$

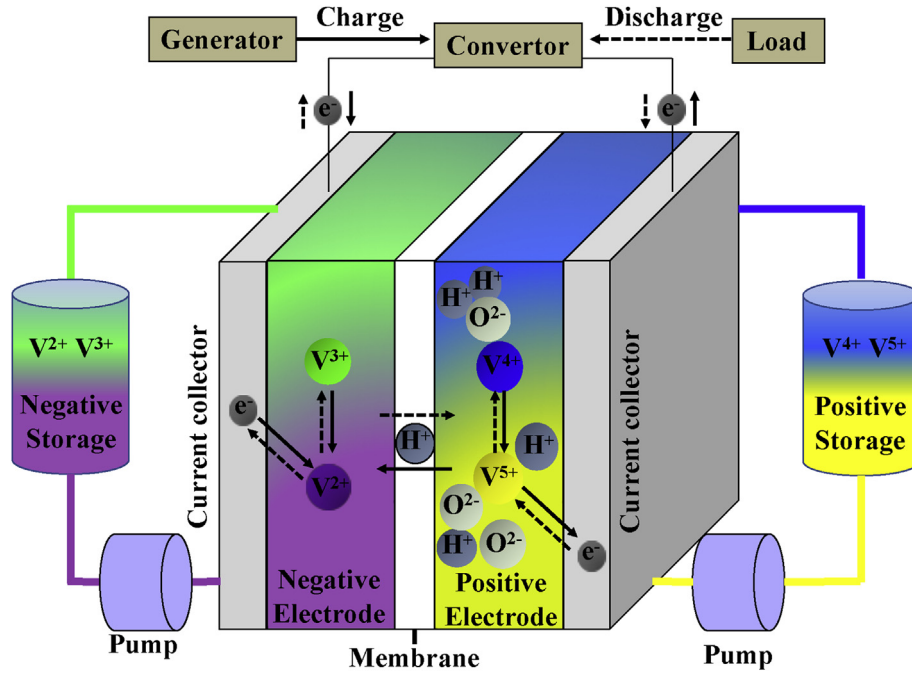


Fig. 1 – Schematic diagram of a single VRFB cell.

where ϕ is the potential, D is the diffusion coefficient, κ is ionic mobility and \vec{u} is the electrolyte velocity. The effective diffusion coefficient of species ($D_{i,eff}$) calculated by the Bruggemann equation as follows.

$$D_{i,eff} = \epsilon^{3/2} D_i \quad (9)$$

The porosity of the electrode (ϵ) is 0.91 and the permeability (K) was calculated by Kozeny-Carman equation [38].

$$K = \frac{d_f^2 \epsilon^3}{K_{ck} (1 - \epsilon)^2} \quad (10)$$

d_f is the fiber diameter and K_{ck} is the Carman-Kozeny constant, which used as a fitting parameter and characterizes the fibrous materials. Meanwhile, the electrolyte flow in the flow field is characterized by incompressible continuity and Navier-Stokes equations.

$$\nabla \cdot \vec{u} = 0 \quad (11)$$

$$\rho(\vec{u} \cdot \nabla) \vec{u} = -\nabla p + \mu \nabla^2 \vec{u} \quad (12)$$

where ρ is the density of the bulk solution while p represents the pressure.

The volumetric transfer current density (j) that describes the vanadium redox reactions in both electrodes, can be calculated by the Butler-Volmer equation as follows [39].

$$j_- = a F k_- (c_{v(II)})^{(1-\alpha_-)} (c_{v(III)})^{\alpha_-} \left[\left(\frac{c_{v(II)}^s}{c_{v(II)}} \right) \exp \left(\frac{(1-\alpha_-) F \eta_-}{RT} \right) - \left(\frac{c_{v(III)}^s}{c_{v(III)}} \right) \exp \left(-\frac{\alpha_- F \eta_-}{RT} \right) \right] \times T \quad (13)$$

(nsfer current density, equation describes the vanadium redox reactions in the electrodes, the electrolyte. nservation equat)

$$j_+ = a F k_+ (c_{v(IV)})^{(1-\alpha_+)} (c_{v(V)})^{\alpha_+} \left[\left(\frac{c_{v(IV)}^s}{c_{v(IV)}} \right) \exp \left(\frac{(1-\alpha_+) F \eta_+}{RT} \right) - \left(\frac{c_{v(V)}^s}{c_{v(V)}} \right) \exp \left(-\frac{\alpha_+ F \eta_+}{RT} \right) \right] \quad (14)$$

It is denoted that the subscripts of $-$ and $+$ are negative and positive parameters. Eqs. (13) and (14) are for the negative and positive electrodes, respectively, where a is the specific surface area of the porous electrode, k represents the redox reaction rate constant, α is the transfer coefficient, η is the overpotential, which can be expressed as:

$$\eta_+ = \phi_{s,+} - \phi_{l,+} - E_{0,+} \quad (15)$$

$$\eta_- = \phi_{s,-} - \phi_{l,-} - E_{0,-} \quad (16)$$

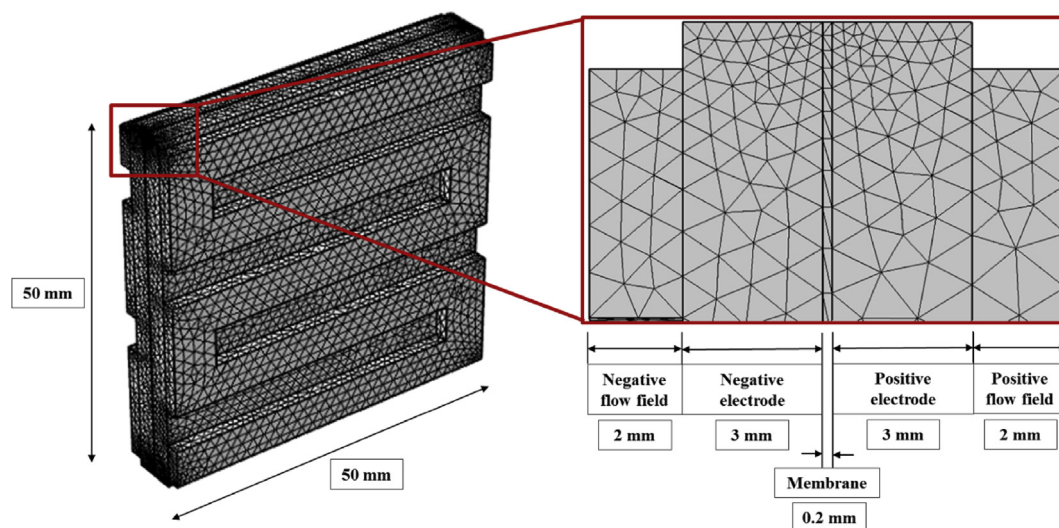
ϕ_l and ϕ_s are the electrolyte and electrode potentials while E_0 represents the equilibrium electrical potential for reactions (1)–(4), which can be given as:

$$E_{0,-} = -0.26 + \frac{RT}{F} \ln \left(\frac{c_{v(III)}}{c_{v(II)}} \right) \quad (17)$$

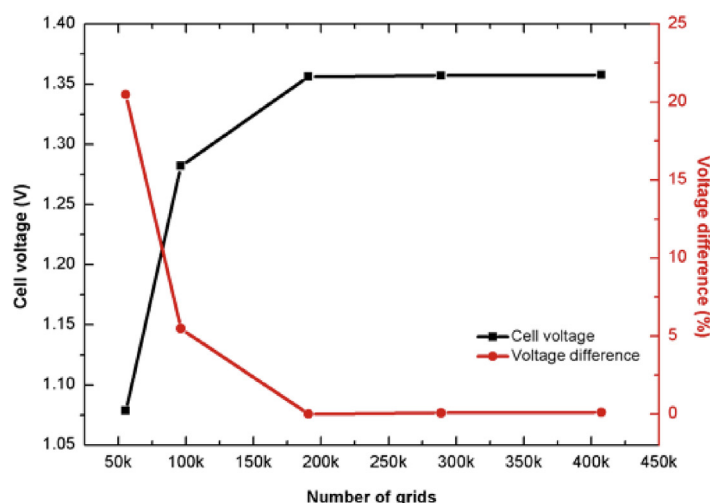
$$E_{0,+} = 1.004 + \frac{RT}{F} \ln \left(\frac{c_{v(V)} \times (c_{H^+})^2}{c_{v(IV)}} \right) \quad (18)$$

Table 1 – Source terms of the governing equations.

Term	Positive electrode	Negative electrode
$V^{2+}, S_{V^{2+}}$	–	j/F
$V^{3+}, S_{V^{3+}}$	–	$-j/F$
$V^{4+}, S_{V^{4+}}$	j/F	–
$V^{5+}, S_{V^{5+}}$	$-j/F$	–
H^+, S_{H^+}	$-2j/F$	–



(a) Generated grids for the numerical simulation of VRFB performance



(b) Grid independency test to determine optimum number of grids

Fig. 2 – The numerical grids generation for the calculation domain in this study. (a) Generated grids for the numerical simulation of VRFB performance. (b) Grid independency test to determine optimum number of grids

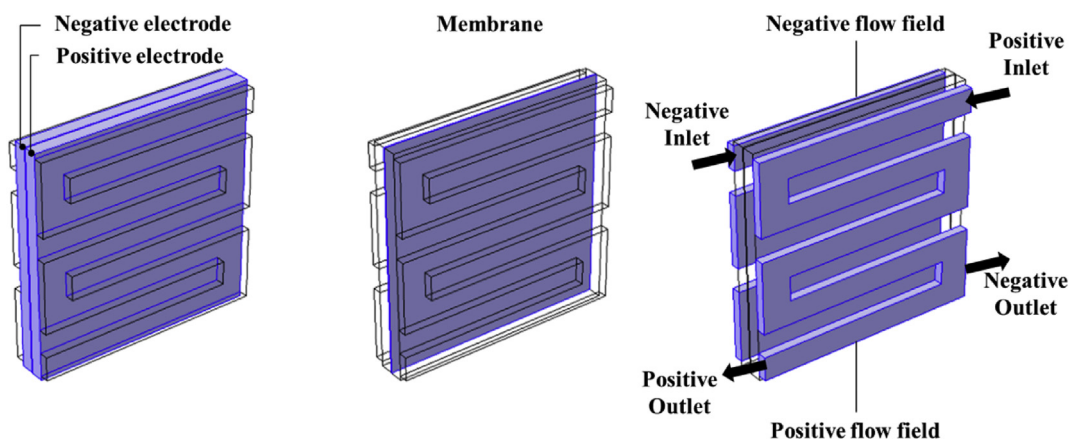


Fig. 3 – VRFB cell structure used for the numerical simulations.

Table 2 – Electrochemical properties.

Property	Value
Porosity	0.91
Kozeny-Carman constant	4.28
Carbon fiber diameter (m)	1.76×10^{-5}
Faraday constant (C mol ⁻¹)	96,485
Universal gas constant (J mol ⁻¹ K ⁻¹)	8.3145
Specific surface area (m ⁻¹)	1.62×10^4
Electrode conductivity (S m ⁻¹)	1000
Viscosity (Pa·s)	4.928×10^{-3}
Density (kg m ⁻³)	1354
V ²⁺ diffusion coefficient (m ² s ⁻¹)	2.4×10^{-10}
V ³⁺ diffusion coefficient (m ² s ⁻¹)	2.4×10^{-10}
V ⁴⁺ diffusion coefficient (m ² s ⁻¹)	3.9×10^{-10}
V ⁵⁺ diffusion coefficient (m ² s ⁻¹)	3.9×10^{-10}
H ⁺ diffusion coefficient (m ² s ⁻¹)	9.312×10^{-9}
SO ₄ ²⁻ diffusion coefficient (m ² s ⁻¹)	1.065×10^{-9}
HSO ₄ ⁻ diffusion coefficient (m ² s ⁻¹)	1.33×10^{-9}
Initial vanadium concentration (mol m ⁻³)	1600
Initial proton concentration (mol m ⁻³)	4000
Initial sulfate concentration (mol m ⁻³)	4500
State of charge (SOC)	0.8

Table 3 – Operating parameters.

Parameters	Value
Negative transfer coefficient	0.45
Positive transfer coefficient	0.55
Negative rate constant (m s ⁻¹)	1.7×10^{-7}
Positive rate constant (m s ⁻¹)	6.8×10^{-7}
Negative standard potential (V)	-0.255
Positive standard potential (V)	1.004
Pump efficiency	0.9

Then the cell voltage can be calculated by using the equilibrium electrical potentials and overpotentials as expressed in Eq. (19).

$$E_{\text{cell}} = E_{0,+} - E_{0,-} + \frac{RT}{F} \ln \frac{c_{\text{V(IV)}} c_{\text{V(III)}} c_{\text{H}^+}^2}{c_{\text{V(III)}} c_{\text{V(IV)}}} - \eta_- - \eta_+ - I A R_{\text{cell}} \quad (19)$$

where I , A , and R_{cell} are electrical current density, surface area and electrical resistance of the cell, respectively.

We have conducted numerical simulations based on the finite-element method. The generated numerical grids and the regions of inlets and outlets are presented in Fig. 2(a) and Fig. 3, respectively. It should be denoted that we have performed grid independency test with varying the number of grids from 55,472 to 407,398. As can be seen in Fig. 2(b), the optimum number of grids is found to 190,790.

Table 4 – Boundary conditions.

Boundary	Value
Positive and negative inlets (mL min ⁻¹)	40, 60, 80, 100
Outlet (bar)	1
Applied current density (mA cm ⁻²)	60
Operating temperature (K)	298

Boundary conditions and parameters

In this numerical model, the electrochemical properties and parameters used to simulate the VRFB performance are listed in Table 2 and Table 3. The mass flow inlet and pressure outlet boundary conditions are specified at the positive and negative flow fields. The concentration of vanadium ions at the inlets can be treated as constant at the given SOC. At the outlets, all the diffusive fluxes are defined to zero. The input values of the boundary conditions for calculating a reference case are summarized in Table 4. We consider 5 different serpentine flow fields to investigate the VRFB performance with respect to the supplied electrolyte flow rate. The schematic diagrams are in Fig. 4. It is denoted that the cross-section of the serpentine flow channel is the square of the given size.

Results and discussion

The numerical model is validated by comparing with the experimental results. Then, the effects of the electrolyte flow rate and the size of serpentine channel are numerically investigated.

Model validation

The numerically predicted voltage of VRFB with zero-gap flow field is validated against the experimental data where the applied current density is 60 mA cm⁻². Electrolyte solutions are prepared in a mixture of V(III) and V(IV) at 1.6 M in 4 M sulfate oxide hydrogen. The details of experimental setup and VRFB cell structure can be found in the previous study [40]. It is noted that the SOC-dependent experimental data are plotted to compare with numerical simulation results. As seen in Fig. 5, our numerical model well predicts the experimental data trend with good accuracy. The small difference between numerical and experimental results can be neglectable when the unavoidable side effect and measurement uncertainty are considered. Thus, the numerical model can be reasonably useful to further investigations on the optimization of the VRFB performance.

Effects of channel size and flow rate on cell voltage

Numerical simulations have been conducted with the variations of serpentine channel size and electrolyte flow rate. It is denoted that the electrolyte solutions and applied electrical current density are same that in the numerical model validation, while the SOC is defined to 0.8. As a result, Fig. 6(a) shows the variation of overpotentials against electrolyte flow rate and serpentine channel size while Fig. 6(b) illustrates the resulting cell voltage at the same conditions. When the electrolyte flow rate is 40 mL min⁻¹, the calculated overpotential is 0.0423 for the serpentine channel size of 9.6 mm. Meanwhile the overpotential is ranged from 0.03 to 0.0322 for the channel size between 1.9 and 5.3 mm. The channel size reduction induces the decreased overpotential resulting in high cell voltage. In addition, the increased electrolyte flow rate also reduces overpotential resulting in increased cell voltage.

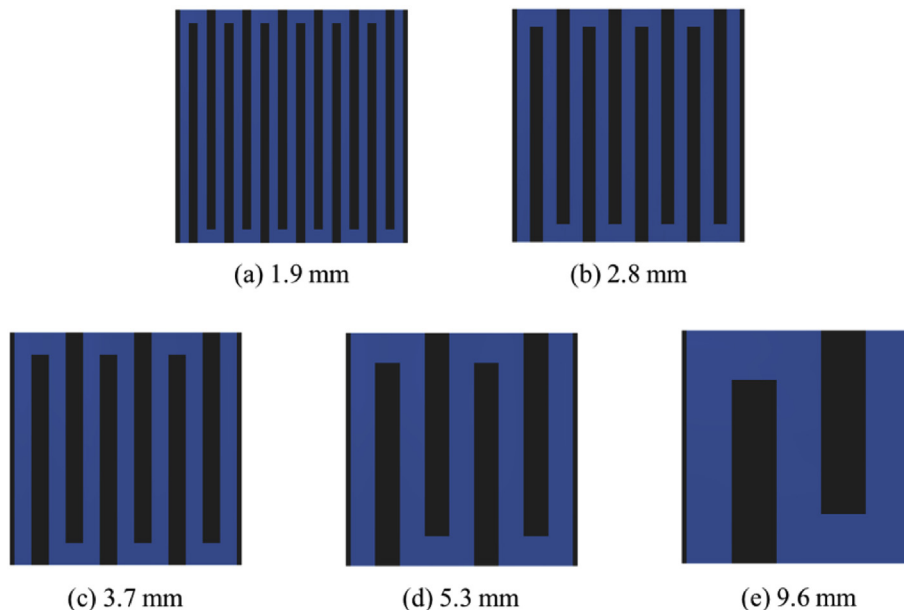


Fig. 4 – Schematic diagrams of 5 different serpentine flow field.

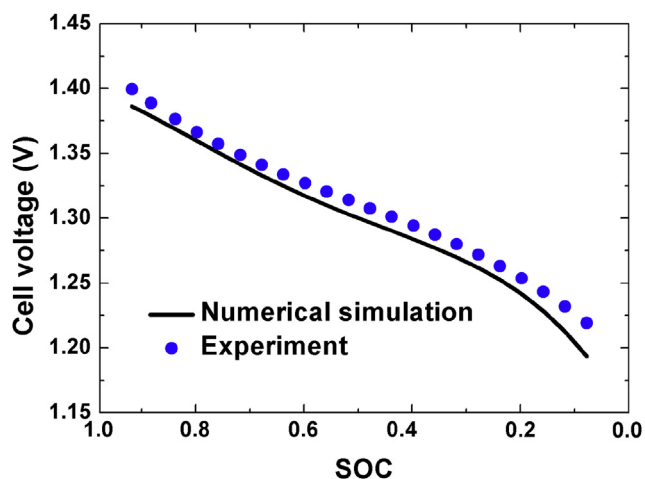


Fig. 5 – Comparison between numerical simulation and experimental data.

When the concentration of $V(II)$, V^{2+} , is taken to display in Fig. 7, it can be clearly seen that the channel size reduction significantly improves the uniformity of the molar concentration. The average molar concentration of $V(II)$ also increases from 1105.4 to 1248.6 mol m^{-3} where channel size decreases from 9.6 to 1.9 mm. The displayed contours of molar concentration indicate that the reduction of serpentine channel size supplies more uniform electrolyte flow through the porous electrode resulting in higher molar concentration. The volumetric transfer current density from Butler-Volmer equations also indicates the inverse relationship between the molar concentration and overpotential as described in Eqs. (13) and (14).

Although the reduced serpentine channel size improves the cell voltage due to increased molar concentration, however, the increased pressure drop is inevitable due to the

reduced channel size. In this regard, the relation between the pressure drop and the channel size for the given electrolyte flow rates needs to be investigated. As can be seen in Fig. 8, the pressure drop significantly is increased up to 1273 Pa when the channel size is 1.9 mm with the flow rate of 60 mL min^{-1} . Meanwhile, the pressure drops are calculated from 71 to 1093 Pa when the channel size is varied from 9.6 to 3.7 mm. The contours of pressure in the serpentine channels imply that the reduced channel size requires more mechanical power to supply the given electrolyte flow rate. In this regard, when a pump is considered to supply the electrolyte, the mechanical power can be calculated for the given flow rate and the obtained pressure drop. In Fig. 9, the calculated pressure drop and pump power against electrolyte flow rate are plotted. It is noted that the pump power should be doubled because two pumps are used to provide electrolyte flow for positive and negative sides. For the given channel size, the linear relationship between pressure drop and flow rate indicates that most of pressure drop occurs in the channel. The channel size of 1.9 mm induces the highest pressure drop of 2286 Pa at 100 mL min^{-1} , while the lowest pressure drop of 169 Pa at 40 mL min^{-1} is calculated for the 9.6 mm in channel size. It can be seen that the significant pressure rise is caused by the increased flow rate and decreased channel size. The resulting pump power is ranged from 0.1 to 7.6 mW.

Optimization of serpentine channel size

The reduced serpentine channel size decreases the overpotential by providing uniform molar concentration at the porous electrode resulting in improved VRFB performance. Nonetheless, the power loss due to the overpotential and consumed pump power should be taken into account to evaluate optimum power generation of the VRFB cell [33,41]. In this regard, the power-based efficiency (ψ_{power}) is defined as follows.

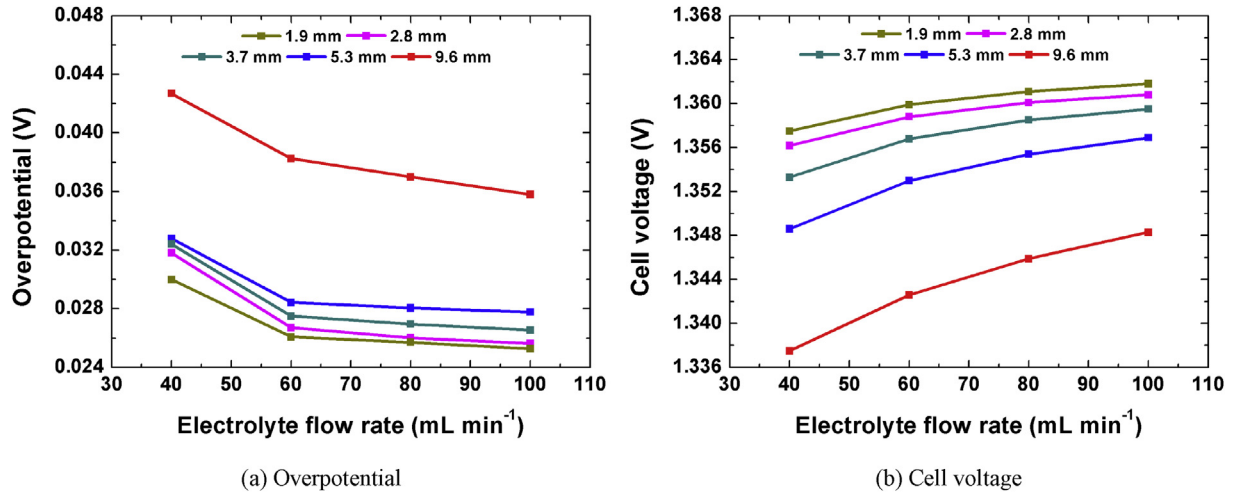


Fig. 6 – The calculated values of overpotential and cell voltage against the electrolyte flow rate and channel size.

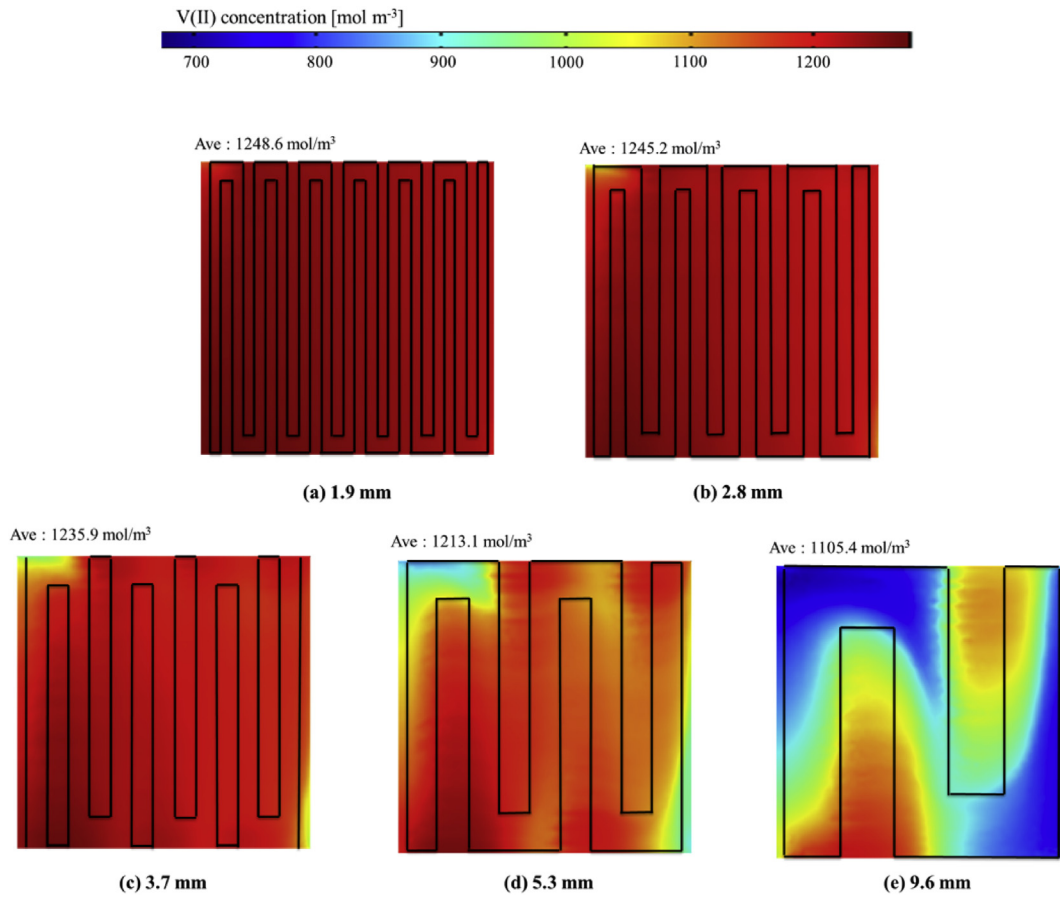


Fig. 7 – The reduced molar concentration of V (II) with increased channel size.

$$\psi_{\text{power}} = \frac{P_{\text{net}}}{P_{\text{total}}} = 1 - \frac{P_{\text{pump}} + P_{\text{loss}}}{P_{\text{total}}} \quad (20)$$

where P_{net} , P_{pump} , P_{loss} , and P_{total} represent net power, pump power, power loss, and total generated power, respectively.

The pump power can be evaluated by the pressure drop (ΔP) for the given flow rate (Q).

$$P_{\text{pump}} = Q \cdot \frac{\Delta P}{\psi_{\text{pump}}} \quad (21)$$

ψ_{pump} is the energy conversion efficiency of pump and

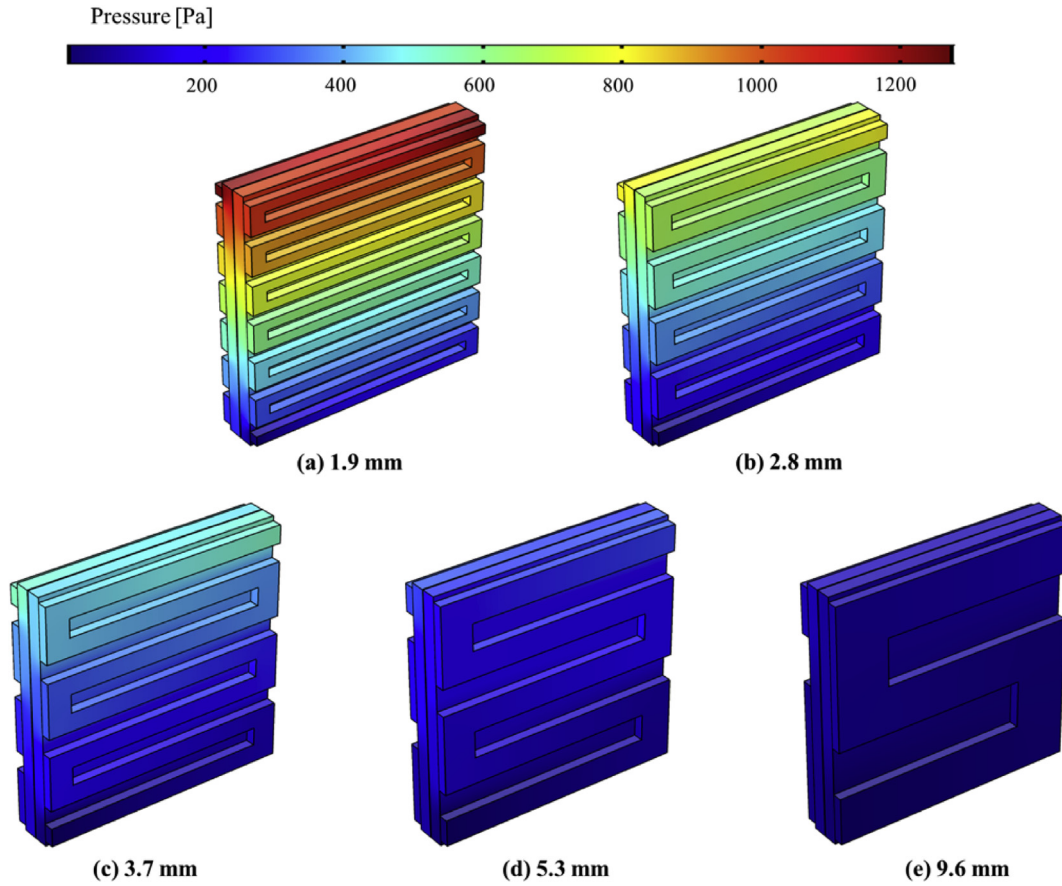


Fig. 8 – Pressure distributions for the different channel sizes.

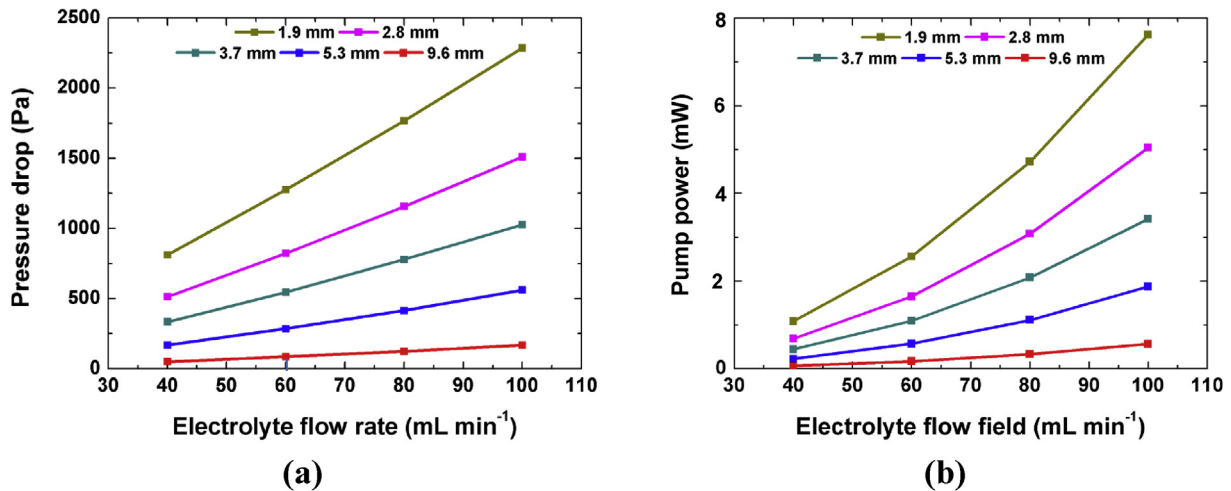


Fig. 9 – (a) Pressure drops and (b) pump power for the channel sizes against electrolyte flow rate.

assumed to 0.9 in this study. The power loss is the sum of the activation loss due to overpotential and ohmic loss through the membrane as expressed in Eq. (22).

$$P_{\text{loss}} = IA(\eta_- + \eta_+) + (\Delta V_{\text{mem}})^2 \cdot \frac{A\sigma_{\text{mem}}}{\delta_{\text{mem}}} \quad (22)$$

Where $\eta_- + \eta_+$ is total overpotential and ΔV_{mem} , σ_{mem} and δ_{mem} represent the voltage difference through the membrane,

electrical conductivity and thickness of membrane, respectively.

The calculated power-based efficiency with respect to the flow rate and channel size are plotted in Fig. 10. It can be seen that the maximum power-based efficiency is 96.6% at the channel size of 1.9 mm and 60 mL min⁻¹. Although the power loss (P_{loss}) is reduced with the increased flow rate above 80 mL min⁻¹, however, the increased pump power induces the

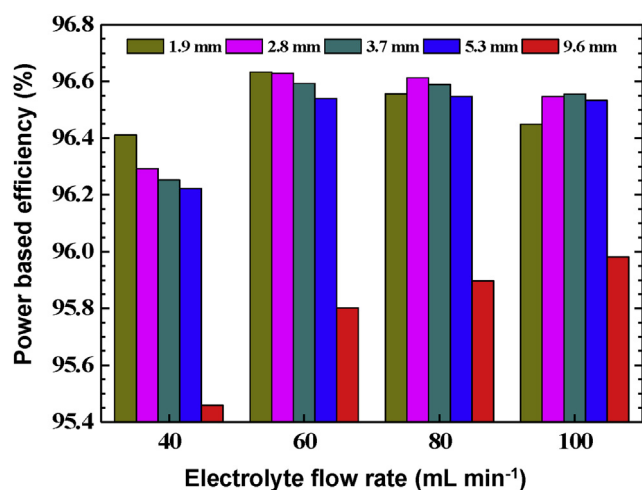


Fig. 10 – Power-based efficiency according to various flow rate and channel size.

net power reduction. Similar trend can be found for the channel size between 2.8 and 5.3 mm. The power-based efficiency continues to increase with the increased flow rate for the channel size of 9.6 mm. As can be seen in Fig. 7(d), the non-uniform distribution of molar concentration is improved with increased flow rate but the power-based efficiency is up to 95.9% at 100 mL min⁻¹.

In this study, we have simulated the effect of channel size on the power-based efficiency of VRFB cell. The reduced channel size with optimum flow rate can be found. Consequently, the maximum power-based efficiency of 96.6% is calculated with the channel size of 1.9 mm at 60 mL min⁻¹.

Conclusions

The three-dimensional numerical model for VRFB has been successfully developed in this study. The effects of electrolyte flow rate and serpentine channel size on the electrochemical performance and power-based efficiency have also been numerically simulated. It has been found that the reduced channel size improves the distribution of molar concentration, however, it also increases the pressure drop to supply the defined electrolyte flow rate. Our numerical simulations suggest that the VRFB with specific channel size and flow rate shows optimum power-based efficiency. The maximum efficiency of 96.6% is achieved when the serpentine channel size is 1.9 mm at the flow rate of 60 mL min⁻¹. It should be denoted that our numerical approach will be highly applicable when the large amount of electrolyte flow rate is required for the commercial-scale VRFB.

Acknowledgements

This work was supported by the National Research Foundation of Korea grant funded by the Korea government (MSIT, NRF-2019R1A2C1002212) and (MSIP, 2018R1A5A6075959).

REFERENCES

- [1] Castillo A, Gayme Dennice F. Grid-scale energy storage applications in renewable energy integration: a survey. *Energy Convers Manag* 2014;87:885–94.
- [2] Dunn B, Kamath H, Tarascon JM. Electrical energy storage for the grid: a battery of choice. *Science* 2011;334:928–35.
- [3] Yang Z, Zhang J, Kintner-Meyer MC, Lu X, Choi D, Lemmon JP, Liu J. Electrochemical energy storage for green grid. *Chem Rev* 2011;111:3577–613.
- [4] Zhang C, Zhao TS, Xu Q, An L, Zhao G. Effects of operating temperature on the performance of vanadium redox flow batteries. *Appl Energy* 2015;155:349–53.
- [5] Turker B, Klein SA, Komsisky L, Trujillo JJ. Utilizing a vanadium redox flow battery to avoid wind power deviation penalties in an electricity market. *Energy Convers Manag* 2013;76:1150–7.
- [6] Knudsen E, Albertus P, Cho KT, Weber AZ, Kojic A. Flow simulation and analysis of high-power flow batteries. *J Power Sources* 2015;299:617–28.
- [7] Wen Y, Xu Y, Cheng J, Cao G, Yang Y. Investigation on the stability of electrolyte in vanadium flow batteries. *Electrochim Acta* 2013;96:268–73.
- [8] Khazaeli A, Vatani A, Tahouni N, Panjeshahi MH. Numerical investigation and thermodynamic analysis of the effect of electrolyte flow rate on performance of all vanadium redox flow batteries. *J Power Sources* 2015;293:599–612.
- [9] Oh K, Won S, Ju H. A comparative study of species migration and diffusion mechanisms in all-vanadium redox flow batteries. *Electrochim Acta* 2015;181:238–47.
- [10] Schreiber M, Harrer M, Whitehead A, Bucsich H, Dragschitz M, Seifert E, Tymciw P. Practical and commercial issues in the design and manufacture of vanadium flow batteries. *J Power Sources* 2012;206:483–9.
- [11] Zhou XL, Zhao TS, An L, Zeng YK, Yan XH. A vanadium redox flow battery model incorporating the effect of ion concentrations on ion mobility. *Appl Energy* 2015;158:157–66.
- [12] Yin C, Gao Y, Guo S, Tang H. A coupled three dimensional model of vanadium redox flow battery for flow field designs. *Energy* 2014;74:886–95.
- [13] Badrinarayanan R, Zhao J, Tseng KJ, Skyllas-Kazacos M. Extended dynamic model for ion diffusion in all-vanadium redox flow battery including the effects of temperature and bulk electrolyte transfer. *J Power Sources* 2014;270:576–86.
- [14] Aaron DS, Liu Q, Tang Z, Grim GM, Papandrew AB, Turhan A, Mench MM. Dramatic performance gains in vanadium redox flow batteries through modified cell architecture. *J Power Sources* 2012;206:450–3.
- [15] Won S, Oh K, Ju H. Numerical studies of carbon paper-based vanadium redox flow batteries. *Electrochim Acta* 2016;201:286–99.
- [16] Leung P, Li X, De Leo'n CP, Berlouis L, Low CJ, Walsh FC. Progress in redox flow batteries, remaining challenges and their applications in energy storage. *RSC Adv* 2012;2:10125–56.
- [17] Skyllas-Kazacos M, Chakrabarti MH, Hajimolana SA, Mjalli FS, Saleem M. Progress in flow battery research and development. *J Electrochem Soc* 2011;158:R55–79.
- [18] Banham-Hall DD, Taylor GA, Smith CA, Irving MR. Flow batteries for enhancing wind power integration. *IEEE Trans Power Syst* 2012;27:1690–7.
- [19] Kear G, Shah AA, Walsh FC. Development of the all-vanadium redox flow battery for energy storage: a review of technological, financial and policy aspects. *Int J Energy Res* 2012;36:1105–20.

- [20] Mohamed M, Leung PK, Sulaiman MH. Performance characterization of a vanadium redox flow battery at different operating parameters under a standardized test-bed system. *Appl Energy* 2015;137:402–12.
- [21] Ma X, Zhang H, Sun C, Zou Y, Zhang T. An optimal strategy of electrolyte flow rate for vanadium redox flow battery. *J Power Sources* 2012;203:153–8.
- [22] Sun C, Chen J, Zhang H, Han X, Luo Q. Investigations on transfer of water and vanadium ions across Nafion membrane in an operating vanadium redox flow battery. *J Power Sources* 2010;195(3):890–7.
- [23] Liu H, Yang L, Xu Q, Yan C. Corrosion behavior of a bipolar plate of carbon–polythene composite in a vanadium redox flow battery. *RSC Adv* 2015;5(8):5928–32.
- [24] Knehr KW, Kumbur EC. Open circuit voltage of vanadium redox flow batteries: discrepancy between models and experiments. *Electrochem Commun* 2011;13(4):342–5.
- [25] Yao C, Zhang H, Liu T, Li X, Liu Z. Carbon paper coated with supported tungsten trioxide as novel electrode for all-vanadium flow battery. *J Power Sources* 2012;218:455–61.
- [26] Yang WW, He YL, Li YS. Performance modeling of a vanadium redox flow battery during discharging. *Electrochim Acta* 2015;155:279–87.
- [27] Zhang Y, Zhou X, Xue R, Yu Q, Jiang F, Zhong Y. Proton exchange membranes with ultra-low vanadium ions permeability improved by sulfated zirconia for all vanadium redox flow battery. layer coated composite membranes for vanadium redox flow battery. *Int J Hydrogen Energy* 2019;44:5997–6006.
- [28] Dassisti M, Cozzolino G, Chimienti M, Rizzuti A, Mastorilli P, L'Abbate P. Sustainability of vanadium redox-flow batteries: benchmarking electrolyte synthesis procedures. *Int J Hydrogen Energy* 2016;41:16477–88.
- [29] Gencten M, Gursu H, Sahin Y. Electrochemical investigation of the effects of V(V) and sulfuric acid concentrations on positive electrolyte for vanadium redox flow battery. *Int J Hydrogen Energy* 2016;41:9868–75.
- [30] Gencten M, Gursu H, Sahin Y. Anti-precipitation effects of TiO_2 and TiOSO_4 on positive electrolyte of vanadium redox battery. *Int J Hydrogen Energy* 2017;42:25608–18.
- [31] Tang A, Bao J, Skyllas-Kazacos M. Studies on pressure losses and flow rate optimization in vanadium redox flow battery. *J Power Sources* 2014;248:154–62.
- [32] Houser J, Clement J, Pezeshki A, Mench M. Influence of architecture and material properties on vanadium redox flow battery performance. *J Power Sources* 2016;302:369–77.
- [33] Xu Q, Zhao T, Zhang C. Performance of a vanadium redox flow battery with and without flow fields. *Electrochim Acta* 2014;142:61–7.
- [34] Xu Q, Zhao TS, Leung P. Numerical investigations of flow field designs for vanadium redox flow batteries. *Appl Energy* 2013;105:47–56.
- [35] Kim DK, Yoon SJ, Lee J, Kim S. Parametric study and flow rate optimization of all-vanadium redox flow batteries. *Appl Energy* 2019;228:891–901.
- [36] Ma X, Huamin Z, Feng X. A three-dimensional model for negative half cell of the vanadium redox flow battery. *Electrochim Acta* 2011;58:238–46.
- [37] Shah AA, Watt-Smith MJ, Walsh FC. A dynamic performance model for redox-flow batteries involving soluble species. *Electrochim Acta* 2008;53(27):8087–100.
- [38] Yin C, Guo S, Fang H, Liu J, Li Y, Tang H. Numerical and experimental studies of stack shunt current for vanadium redox flow battery. *Appl Energy* 2015;151:237–48.
- [39] Zhou XL, Zhao TS, An L, Zeng YK, Wei L. Modeling of ion transport through a porous separator in vanadium redox flow batteries. *J Power Sources* 2016;327:67–76.
- [40] Kim J, Park H. Experimental analysis of discharge characteristics in vanadium redox flow battery. *Appl Energy* 2017;206:451–7.
- [41] Blanc C, Rufer A. Optimization of the operating point of a vanadium redox flow battery. *Energy Conversion Congress and Exposition*; 2009. p. 2600–5.